

A Versatile and Accurate Method for Halo Mass Determination from Phase-Space Distribution of Satellite Galaxies

ZHAO-ZHOU LI,^{1,*} YONG-ZHONG QIAN,^{2,3} JIAXIN HAN,^{1,4,†} WENTING WANG,^{4,1} AND Y. P. JING^{1,3,‡}

¹*Department of Astronomy, School of Physics and Astronomy, Shanghai Jiao Tong University, 800 Dongchuan Road, Shanghai 200240, China*

²*School of Physics and Astronomy, University of Minnesota, Minneapolis, MN 55455, USA*

³*Tsung-Dao Lee Institute, Shanghai Jiao Tong University, 800 Dongchuan Road, Shanghai 200240, China*

⁴*Kavli IPMU (WPI), UTIAS, The University of Tokyo, Kashiwa, Chiba 277-8583, Japan*

ABSTRACT

We propose a versatile and accurate method to estimate the halo mass and concentration from the kinematics of satellite galaxies. We construct the 6D phase-space distribution function of satellites from a cosmological simulation based on the similarity of internal dynamics for different halos. Within the Bayesian statistical framework, not only can we infer the halo mass and concentration efficiently, but also treat various observational effects, including the selection function, incomplete data, and measurement errors, in a rigorous and straightforward manner. Through tests with mock samples, we show that our method is valid and accurate, and more precise than pure steady-state methods. It can constrain the halo mass to within $\sim 20\%$ using only 20 tracers and has a small intrinsic uncertainty of $\sim 10\%$. In addition to the clear application to the Milky Way and similar galaxies, our method can be extended to galaxy groups or clusters.

Keywords: galaxies: halos — galaxies: kinematics and dynamics — dark matter — methods: statistical — methods: numerical

1. INTRODUCTION

In this paper we present a method to determine the mass of a dark matter halo using its satellite systems as dynamical tracers. We focus on halos of galactic scale. The halo mass of a galaxy plays a critical role in connecting observations to theoretical understandings based on the underlying matter distribution (see e.g., Wechsler & Tinker 2018), and the halo mass of our own Milky Way (MW) is of particular interest. Various methods have been applied to estimate the halo mass (see Courteau et al. 2014 and Pratt et al. 2019 for general reviews, and Wang et al. 2015; Wang et al. 2019 in preparation for a comprehensive summary of recent estimates for the MW). These methods are suitable for different scopes and probe different aspects of the mass distribution. Among them, dynamical modeling with tracers is perhaps one of the most direct approaches. The mass distribution of the inner halo can be probed by the kinematics of such tracers as stars, planetary nebulae, and globular clusters. All of the above tracers, however, are generally limited in distance from the halo center. In addition, it was shown that stars could be

stochastically-biased tracers for the total halo mass due to incomplete phase-mixing (e.g., Han et al. 2016b; Wang et al. 2017, 2018). Because satellite galaxies have an extended spatial distribution and can be more easily observed out to large distances by current surveys, they are expected to be better tracers for the outer halo, especially if one is interested in measuring the total halo mass (see Han et al. (2019) for more detailed discussions).

Previous approaches to dynamical modeling with satellite systems include the virial theorem (e.g., Biviano et al. 2006; Saro et al. 2013; Tempel et al. 2014), the caustic method (e.g., Diaferio & Geller 1997; Serra et al. 2011; Gifford et al. 2013), the Jeans equation (e.g., Łokas 2002; Evans et al. 2003; Watkins et al. 2010; More et al. 2011; Mamon et al. 2013), and the phase-space distribution function (DF) (e.g., Wilkinson & Evans 1999; Wojtak et al. 2009). Readers are referred to Old et al. (2015) and Armitage et al. (2019) for systematic comparisons of these approaches and to e.g., Watkins et al. (2010) and Eadie et al. (2015) for application of the latter two methods to estimate the MW halo mass. In view of the limited number of satellite galaxies, the associated substantial statistical uncertainties, and the observational errors, it is reasonable to make appropriate assumptions to simplify the modeling, even at the risk of introducing systematic uncertainties. Several or all of the following assumptions are

* lizz.astro@gmail.com
† jiaxin.han@sjtu.edu.cn
‡ ypjing@sjtu.edu.cn

commonly made for the above methods: dynamical equilibrium, spherical symmetry, a velocity anisotropy profile, and a specific form of the DF.

A nearly minimal but very effective assumption is that satellite galaxies are in approximate dynamical equilibrium with their host halo, and therefore, their kinematics can be described by a steady-state phase-space DF. While this assumption is supported by cosmological simulations, understanding the pertinent DF is a long-standing problem (Lynden-Bell 1967). Despite many analytical and empirical (simulation-based) attempts (e.g., Wilkinson & Evans 1999; Evans & An 2006; Wojtak et al. 2008; Williams & Evans 2015; Posti et al. 2015), an accurate and explicit form of the DF for satellite kinematics remains to be found and verified. As shown by Wang et al. (2015) and Han et al. (2016b), introducing unjustified assumptions into the construction of the DF may lead to substantially biased results. When the 6D phase space coordinates of the tracers are available, a promising solution is to use the observed data directly to construct a data-driven DF. An example is the oPDF (orbital probability DF) method (Han et al. 2016c). In some other cases, numerical simulations can be used to provide non-parametric templates as empirical DFs.

In a previous study by Li et al. (2017), the probability density function in the (E, L) space, $d^2N/(dEdL) = p(E, L)$, where E and L are the energy and angular momentum per unit mass, respectively, was derived for satellite galaxies directly from cosmological simulations. It was assumed that the internal dynamics of different halos is similar after the radius and velocity are normalized by their virial scales. By using the $p(E, L)$ for suitable subhalos of a representative template halo, the mass of any other test halo can be determined with good accuracy from the kinematic data on a relatively small number of satellites (see also Callingham et al. 2019). We note, however, that the adopted $p(E, L)$ introduces a bias in the halo mass estimate, which can be overcome by a simple correction factor. This bias arises because E is not a direct observable. As we show in this paper, the use of the proper DF, $d^6N/(d^3\mathbf{r}d^3\mathbf{v}) = f(\mathbf{r}, \mathbf{v})$, which is in terms of the direct observables (position and velocity vectors, \mathbf{r} and \mathbf{v} , respectively) and related to $p(E, L)$ by transformation of variables, gives an unbiased estimate of the halo mass, M .

The improved method presented here builds upon the previous work of Li et al. (2017), but uses the proper DF. It can be understood as a combination of the template-based method of Li et al. (2017) and the oPDF method of Han et al. (2016c). The new method assumes a Navarro-Frenk-White (NFW, Navarro et al. 1996) density profile for the total mass distribution in a halo. The universality of this profile supports the similarity of internal dynamics of halos. Further, the parameters characterizing the NFW profile provide the natural

scales for normalizing the \mathbf{r} and \mathbf{v} of satellites so that the above similarity can be exhibited. Using this similarity, we generalize the simulation-based DF to halos with any set of (M, c) , where c is the concentration parameter for the NFW profile. Consequently, this DF provides estimates of both the halo mass and concentration, from which the mass distribution can be obtained. In addition, it facilitates a proper and straightforward treatment of various observational effects, including selection functions, incomplete measurement (e.g., lack of proper motion), and observational errors.

Due to diversities in formation history and environment, individual halos are expected to exhibit deviations from our assumed DF. This halo-to-halo scatter represents the systematic uncertainty introduced by our assumptions. Using a large mock sample of realistic halos from a cosmological simulation, we demonstrate the validity of our method and quantify its systematic uncertainty. While the major motivation for this work is to estimate the mass of the MW halo with better precision (see e.g., Wang et al. 2019 in preparation for recent estimates and uncertainties), the method in principle can be extended to any halos, including galaxy clusters.

The layout of this paper is as follows. We outline our method in Section 2 and show how to construct the simulation-based DF of satellite kinematics in Section 3. We test the validity and precision of our method using mock samples and make comparisons with other methods in Section 4. We discuss applications of our method in Section 5. Further discussion and conclusions are given in Section 6.

2. OUTLINE OF THE METHOD

As is true of dynamical modeling in general, an accurate statistical description of the satellite kinematics is essential to our method of estimating the halo mass. Our description is based on the following assumptions:

- (1) All halos have the spherical NFW density profile

$$\rho(r) = \frac{\rho_s}{(r/r_s)(1+r/r_s)^2}, \quad (1)$$

where r is the radius, and ρ_s and r_s are the characteristic scales for density and radius, respectively;

- (2) The satellites are in dynamical equilibrium with its host halo and their kinematics in terms of the radial vector, \mathbf{r} , and velocity, \mathbf{v} , can be described by a steady-state DF in phase space

$$\frac{d^6N}{d^3\mathbf{r}d^3\mathbf{v}} = f(\mathbf{r}, \mathbf{v}), \quad (2)$$

which is normalized as $\int f(\mathbf{r}, \mathbf{v})d^3\mathbf{r}d^3\mathbf{v} = 1$;

- (3) The internal dynamics of all halos are similar after \mathbf{r} and \mathbf{v} are normalized by their characteristic scales, r_s and $v_s = r_s\sqrt{4\pi G\rho_s}$, respectively, where G is the gravitational constant.

For a spherical system with a stationary potential, the orbit of a tracer can be specified by the energy per unit mass,

$$E = \frac{1}{2}(v_r^2 + v_t^2) + \Phi(r), \quad (3)$$

and the angular momentum per unit mass, $L = r v_t$, of the tracer, where v_r and v_t are the radial and tangential components of its velocity, respectively. In Equation (3),

$$\Phi(r) = v_s^2 \left[1 - \frac{\ln(1 + r/r_s)}{r/r_s} \right], \quad (4)$$

with $\Phi(0) = 0$, is the gravitational potential¹ corresponding to the NFW profile.

Because only (\mathbf{r}, \mathbf{v}) can be obtained directly from observations, the probability density function in the 6D phase space of (\mathbf{r}, \mathbf{v}) , $d^6N/(d^3\mathbf{r}d^3\mathbf{v}) = f(\mathbf{r}, \mathbf{v})$, instead of that in the 2D (E, L) space, $d^2N/(dEdL) = p(E, L)$, is the proper DF to use in a maximum likelihood estimate of the halo properties from the kinematics of satellites. We will construct $f(\mathbf{r}, \mathbf{v})$ from a cosmological simulation. Due to the limited number of satellites for MW-like halos in this simulation, however, it is difficult to obtain an accurate $f(\mathbf{r}, \mathbf{v})$ directly from the representation of satellites in the 6D phase space of (\mathbf{r}, \mathbf{v}) . It is more practical to first construct $p(E, L)$ from the representation in the 2D (E, L) space based on the simulation, and then use Equation (8) below to convert $p(E, L)$ into $f(\mathbf{r}, \mathbf{v})$. For clarity and convenience, we will refer to $f(\mathbf{r}, \mathbf{v})$ as the DF and $p(E, L)$ as the orbital distribution.

Assuming spherical symmetry, we can decompose the DF $f(\mathbf{r}, \mathbf{v})$ into the orbital distribution $p(E, L)$ and the radial distribution $p(r|E, L)$ along the orbit with a specific set of (E, L) ,

$$f(\mathbf{r}, \mathbf{v}) = \frac{|v_r|}{8\pi^2 L} p(r|E, L) p(E, L), \quad (5)$$

where the first term on the right-hand side comes from the Jacobian for transformation of variables (see Appendix A for details). Under the steady-state assumption (see e.g., Han et al. 2016c),

$$p(r|E, L) dr = \frac{dr}{|v_r(r, E, L)| T_r(E, L)}, \quad (6)$$

where $v_r(r, E, L) = \pm \sqrt{2[E - \Phi(r)] - L^2/r^2}$ is the radial velocity,

$$T_r(E, L) = 2 \int_{r_{\text{peri}}}^{r_{\text{apo}}} \frac{dr}{|v_r(r, E, L)|} \quad (7)$$

¹ Our choice of $\Phi(0) = 0$ gives a more consistent definition of the potential, which makes it easier to compare or combine the DFs for distinct isolated halos. For example, two isolated halos with identical internal density profiles but surrounded by different spherical mass distributions have identical internal dynamics, for which it is more appropriate to use identical potentials. Our choice gives the same potential for both halos, but the common choice of $\Phi(\infty) = 0$ does not.

is the radial orbital period for a specific set of (E, L) , and r_{peri} and r_{apo} are the radii at the pericenter and apocenter, respectively. So we obtain

$$f(\mathbf{r}, \mathbf{v}) = \frac{p(E, L)}{8\pi^2 L T_r(E, L)}. \quad (8)$$

As we can see, the DF $f(\mathbf{r}, \mathbf{v})$ can be fully specified in terms of two isolating integrals, E and L , in accordance with Jeans theorem (section 4.2 of Binney & Tremaine 2008). Mathematically, $f(\mathbf{r}, \mathbf{v})$ only depends on (r, v_r, v_t) under our assumption of spherical symmetry. So we can write $f(\mathbf{r}, \mathbf{v}) = f(r, v_r, v_t)$ by dropping the irrelevant variables. On the other hand, E is a function of (r, v_r, v_t) and L is a function of (r, v_t) . Therefore, Jeans theorem dictates that the dependence of $f(r, v_r, v_t)$ on (r, v_r, v_t) can only be in terms of $E(r, v_r, v_t)$ and $L(r, v_t)$. With this understanding, we write, for convenience,

$$f(\mathbf{r}, \mathbf{v}) = f(r, v_r, v_t) = f(E, L). \quad (9)$$

Because the DF $f(\mathbf{r}, \mathbf{v})$ contains the information on both the orbital distribution $p(E, L)$ and the radial distribution $p(r|E, L)$ for each orbit, we expect that the DF method may constrain halo properties better than other methods based on less information (see Section 4.5).

Under our assumption (3), both $p(E, L)$ and $f(E, L)$ have similar forms for all halos after \mathbf{r} and \mathbf{v} are normalized by the characteristic scales r_s and v_s , respectively. In other words, using the dimensionless variables $\tilde{r} = r/r_s$, $\tilde{v}_r = v_r/v_s$, $\tilde{v}_t = v_t/v_s$, and others derived from them, such as $\tilde{E} = E/v_s^2$ and $\tilde{L} = L/(r_s v_s)$, we can obtain the dimensionless $\tilde{p}(\tilde{E}, \tilde{L})$ and $\tilde{f}(\tilde{E}, \tilde{L})$ that are universal to all halos. The normalization $\int \tilde{f}(\tilde{E}, \tilde{L}) d^3\tilde{r} d^3\tilde{v} = \int f(E, L) d^3\mathbf{r} d^3\mathbf{v} = 1$ requires

$$f(E, L) = \frac{1}{r_s^3 v_s^3} \tilde{f}(\tilde{E}, \tilde{L}). \quad (10)$$

For a halo corresponding to the NFW profile with characteristic scales r_s and v_s , we define its mass, M , and the associated virial radius, R , so that the mean density within R is 200 times the critical density of the present universe. It is straightforward to show that

$$v_s^2 = \frac{GM}{R} \left[\frac{\ln(1+c)}{c} - \frac{1}{1+c} \right]^{-1}, \quad (11)$$

where $c = R/r_s$ is the concentration of the halo. Therefore, M and c are equivalent to r_s and v_s . To emphasize that the halo properties are estimated from the raw kinematic data through the proper DF discussed here, we denote this essential input to our method as

$$p(\mathbf{w}|M, c) = f(E, L), \quad (12)$$

where \mathbf{w} is a shorthand for (\mathbf{r}, \mathbf{v}) .

2.1. Estimate of halo properties

Consider a sample of N_{tracer} satellites with mutually independent kinematic data $\{\mathbf{w}_i, i = 1, \dots, N_{\text{tracer}}\}$. Using the DF discussed above, we can write the probability of observing such a sample for a halo of mass, M , and concentration, c , as

$$p(\{\mathbf{w}_i\}|M, c) = \prod_{i=1}^{N_{\text{tracer}}} p(\mathbf{w}_i|M, c). \quad (13)$$

The best-fit values of (M, c) can then be inferred from the maximum likelihood method with the Bayesian formula

$$p(M, c|\{\mathbf{w}_i\}) \propto p(\{\mathbf{w}_i\}|M, c)p(c|M)p(M), \quad (14)$$

where $p(M)$ and $p(c|M)$ represent our prior knowledge of the halo. For a random halo in the universe, the halo mass function and the mass-concentration relation are the natural choices for these two priors. One can also use a flat prior to avoid relying on extra information.

2.2. Inclusion of observational effects

Real data suffer from various observational effects, such as incompleteness due to sample selection, lack of certain measurements (e.g., proper motion), and observational errors. It is straightforward to include these effects in deriving the proper DF. We give two types of examples below.

2.2.1. Selection function

For a sample restricted by the selection function $S(\mathbf{w})$, the DF is given by

$$p_s(\mathbf{w}|M, c) = \frac{p(\mathbf{w}|M, c)S(\mathbf{w})}{\int p(\mathbf{w}'|M, c)S(\mathbf{w}')d^6\mathbf{w}'}, \quad (15)$$

where $d^6\mathbf{w}'$ is a shorthand for $d^3\mathbf{r}'d^3\mathbf{v}'$. The selection function $S(\mathbf{w}) \leq 1$ indicates the degree of completeness by specifying how likely a satellite with the kinematic data \mathbf{w} is observed. A simple example is a sample that is complete within some distance. More realistically, because observations of satellites are restricted by the limiting magnitude of the survey (e.g., Jethwa et al. 2018), less luminous satellites are observed out to smaller distances.

2.2.2. Incomplete data

It is very difficult to measure the tangential velocity (proper motion) for distant satellites of the MW, not to mention satellites of extragalactic systems. The radial velocity might also be absent, as its measurement requires high-quality spectrum, and hence, expensive time on large telescopes. To maximize the use of all available data and improve the estimates, we can

include satellites with incomplete data by marginalizing the DF. For those without v_t or v_r , the marginalized DF is

$$p(\mathbf{r}, v_r|M, c) = 2\pi \int f(r, v_r, v_t)v_t dv_t, \quad (16)$$

$$p(\mathbf{r}, v_t|M, c) = \int f(r, v_r, v_t)dv_r, \quad (17)$$

respectively. Note for example, that $p(\mathbf{r}, v_r|M, c)$ is evaluated at fixed (r, v_r) , which, along with the integration variable v_t , determine the input (E, L) for $f(r, v_r, v_t) = f(E, L)$.

From a theoretical perspective, previous studies (e.g., Binney & Tremaine 2008; Wojtak et al. 2008) showed that the mass distribution of a spherical system is mainly determined by the energy distribution of its constituents, but is insensitive to their velocity anisotropy or angular momentum distribution. Therefore, we may obtain good estimates of the halo properties by using the marginalized DF for the total velocity $v_{\text{tot}} = \sqrt{v_r^2 + v_t^2}$, which is given by

$$\begin{aligned} p(\mathbf{r}, v_{\text{tot}}|M, c) &= 2\pi \int \delta(v_{\text{tot}} - \sqrt{v_r^2 + v_t^2})f(r, v_r, v_t)v_t dv_t dv_r \\ &= 2\pi v_{\text{tot}} \int_{-v_{\text{tot}}}^{v_{\text{tot}}} f\left(r, v_r, \sqrt{v_{\text{tot}}^2 - v_r^2}\right)dv_r. \end{aligned} \quad (18)$$

The above results are applied in Section 4.4 to discuss the effects of individual observables on the estimates of halo properties.

3. CONSTRUCTION OF PHASE-SPACE DISTRIBUTION

We now present the details of constructing the DF of satellites in the phase space of (\mathbf{r}, \mathbf{v}) based on a cosmological simulation.

3.1. Halo sample

We use a large sample of halos selected from a cosmological N-body (dark matter only) simulation, the Millennium II (Boylan-Kolchin et al. 2009). A similar sample was used to study the systematics of dynamical modeling in Wang et al. (2017, 2018). The Millennium II simulation has a box size of $100h^{-1}\text{Mpc}$ and a particle mass of $m_p = 6.9 \times 10^6 h^{-1}M_\odot$. It adopts the first-year WMAP cosmology (Spergel et al. 2003) with $\Omega_m = 0.25$, $\Omega_\Lambda = 0.75$, $h = 0.73$, $n_s = 1$, and $\sigma_8 = 0.9$.

We identify a sample of halos with $11.5 \leq \lg M/M_\odot \leq 12.5$ that are analogous to the MW in mass.² As shown in Li et al. (2017), the influence of a massive neighbor (e.g., M31) on satellite kinematics is small when the neighbor is

² For ease of comparison with results in the literature, we define the halo mass, M , and the associated virial radius, R , so that the mean density within R is 200 times the critical density of the present universe.

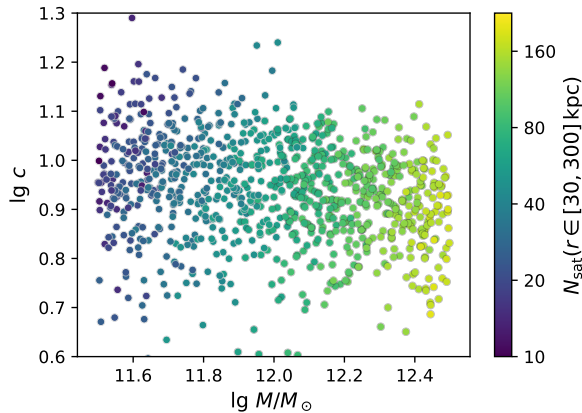


Figure 1. Fitted values of the halo mass, M , and concentration, c , for our halo sample based on the NFW profile. Each dot represents a halo and is colored according to the number of satellites in the radial range of $r = 30\text{--}300$ kpc from the halo center.

at a distance exceeding 3 times its virial radius. To exclude potential influence of nearby massive neighbors, we select isolated halos by requiring that all companions within a sphere of 2 Mpc in radius are at least an order of magnitude smaller in mass. In the end, we have 943 isolated halos, each of which contains $\sim 10^5$ particles.

We fit the NFW density profile to each halo in the sample. The fitted values of the halo mass, M , and concentration, c , are shown in Figure 1. The NFW profile is a good fit in general, with differences of $\lesssim 3\%$ between the fitted M and the true values. We drop 3 halos with uncommonly small values of $c < 3.5$. The concentration parameters of the remaining 940 halos follow a log-normal distribution with a slight dependence on the halo mass. We take this result as the default prior for c :

$$p(\lg c|M) = \mathcal{N}(0.94 - 0.077 \lg(M/10^{12} M_\odot), 0.11). \quad (19)$$

The above result is consistent with previous studies (e.g., Dutton & Macciò 2014). The halos in the final sample have characteristic radial scales of $r_s \sim 20\text{--}40$ kpc. As discussed in Section 2, we will use the r_s and $v_s = r_s \sqrt{4\pi G \rho_s}$ associated with the NFW profile to obtain dimensionless variables such as $\tilde{r} = r/r_s$ and $\tilde{v}_r = v_r/v_s$.

3.2. Satellite samples

Based on the Millennium II simulation, Guo et al. (2011) generated a galaxy catalog using the semi-analytical model (SAM) for galaxy formation. We select satellites from this catalog, which includes orphan satellites whose parent subhalos are eventually disrupted. We only use satellites with stellar masses of $m_\star \geq 100 M_\odot$ whose parent subhalos have infall masses of $M_{\text{inf}} \geq 30 m_p$.

We select a sample of 104,315 satellites with radii $r \leq 25 r_s$ (measured from the respective host halo centers), hereafter

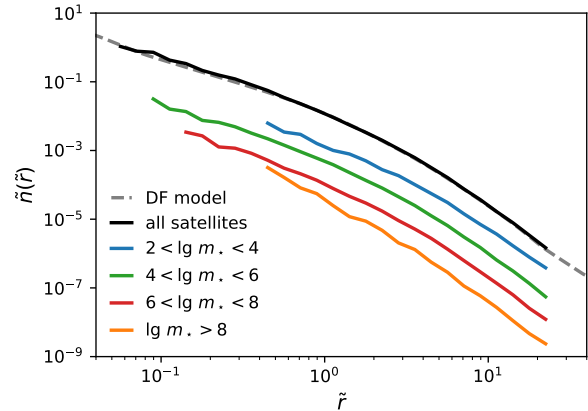


Figure 2. The spatial distributions of satellites with $\tilde{r} = r/r_s \leq 25$ in the template sample. The black solid curve shows the normalized dimensionless number density \tilde{n} as a function of \tilde{r} for all of the selected satellites. This result is reproduced very well by the dashed gray curve derived from the simulation-based DF. The colored curves show the distributions for satellites with different stellar masses. These curves are shifted in amplitude for better comparison. The true distributions are truncated at the inner radius bin that contains fewer than 10 satellites. They show little dependence on stellar masses of satellites for $\tilde{r} > 1$.

referred to as the template sample, to construct the DF in the phase space of (\mathbf{r}, \mathbf{v}) . The Hubble flow is included when we calculate the \mathbf{v} for satellites relative to their host halos, but this inclusion only makes a small difference. Combining the statistics on satellites with the same dimensionless $\tilde{r} = r/r_s$, we show their spatial distributions in Figure 2. It can be seen that these distributions depend very little on stellar masses of satellites, at least for $\tilde{r} > 1$. Although not shown in Figure 2, the spatial distributions of satellites for $\tilde{r} > 1$ do not depend on infall masses of their parent subhalos, either. These results are consistent with those in literature (e.g., Han et al. 2016a; Newton et al. 2018) and suggest that selection based on satellite luminosity or mass may not introduce any significant bias.

To mimic observations of the MW satellites, we make mock samples of satellites for individual halos by selecting only those satellites with $30 \leq r \leq 300$ kpc. The number of such satellites for each halo ranges from ~ 10 to 200, and is shown by the color coding in Figure 1.

3.3. Phase-space distribution

Following our assumptions in Section 2, especially the one regarding the similarity of internal dynamics for different halos, we construct the dimensionless DF in phase space, $\tilde{f}(\tilde{E}, \tilde{L})$, by combining the statistics on the satellites in the template sample. The validity of our assumptions is discussed in Appendix B and ultimately tested by applying the above DF to estimate halo properties of mock samples in Section 4.

Details of constructing the DF are given in Appendix C. A similar procedure was used in [Callingham et al. \(2019\)](#), but to construct $\tilde{p}(\tilde{E}, \tilde{L})$ only.

It is worthwhile to point out some subtlety in constructing $\tilde{f}(\tilde{E}, \tilde{L})$. As defined in Equation (7), the radial orbital period $T_r(E, L)$ used for the construction corresponds to $r_{\text{peri}} \leq r \leq r_{\text{apo}}$ in general. However, because the satellites in the template sample have $r \leq r_{\text{lim}} = 25r_s$, the upper limit for the radial integral in Equation (7) should be replaced by the smaller of r_{lim} and r_{apo} . Nevertheless, it is important to recognize that the DF constructed from this sample, $\tilde{f}(\tilde{E}, \tilde{L})$, is a function of \tilde{E} and \tilde{L} only, and is not subject to any radial limit. In other words, so long as our assumptions are valid, all satellites with different (\tilde{r}, \tilde{v}) but the same (\tilde{E}, \tilde{L}) are described by $\tilde{f}(\tilde{E}, \tilde{L})$. (If the steady-state assumption is not satisfied everywhere, the obtained DF is essentially the average within r_{lim} for a halo.)

Our simulation-based DF, $\tilde{f}(\tilde{E}, \tilde{L})$, is shown in Figure 3. This DF of satellites is very similar to that obtained by [Wojtak et al. \(2008\)](#) for dark matter particles in simulated cluster halos. In both cases, the DF depends largely on \tilde{E} and is not very sensitive to \tilde{L} . Note that our DF covers unbound satellites,³ which constitute $\approx 0.35\%$ of the template sample. Therefore, in using this DF to estimate the properties of a halo, no assumption needs to be made regarding whether any satellite is bound to it or not (e.g., Leo I for the MW).

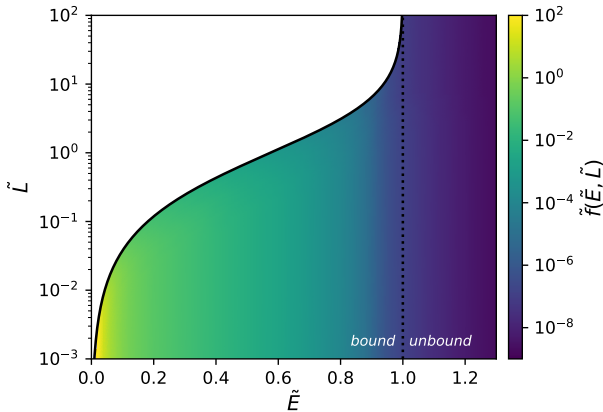


Figure 3. Dimensionless DF in phase space, $\tilde{f}(\tilde{E}, \tilde{L})$, constructed from the template sample of satellites. Note that satellites with $\tilde{E} > 1$ (to the right of the dotted line) are not bound.

As a simple test of consistency, we calculate the dimensionless density profile for the satellites in the template sample,

$$\tilde{n}(\tilde{r}) = 2\pi \int \tilde{f}(\tilde{E}, \tilde{L}) \tilde{v}_t d\tilde{v}_t d\tilde{v}_r, \quad (20)$$

³ All tracers need not be bound to their host halo in a steady state, which only requires them to be uniformly distributed in phase angles along the orbits ([Han et al. 2016c](#)).

where v_t is integrated from 0 to ∞ and v_r from $-\infty$ to ∞ . As shown in Figure 2, the above result is in excellent agreement with the true profile.

4. VALIDATION WITH MOCK TESTS

We test the validity and accuracy of our method for estimating the halo mass, M , and concentration, c , using the mock samples of satellites described in Section 3.2. For each test halo (see Section 3.1), we estimate its properties by choosing a random subset of its satellites as observed tracers. Because the satellites in the mock samples have $30 \leq r \leq 300$ kpc, the proper DF to use (see Section 2.2.1) is

$$p_s(\mathbf{w}|M, c) = \frac{p(\mathbf{w}|M, c)}{\int_{30 \leq r' \leq 300 \text{ kpc}} p(\mathbf{w}'|M, c) d^6 \mathbf{w}'}. \quad (21)$$

The above DF is used in Equation (14) to estimate halo properties with a flat prior in terms of $\lg M$. The default prior on c is given in Equation (19). We also present results for a flat prior in terms of $\lg c$.

4.1. Example application to a halo

We randomly picked a halo from the sample described in Section 3.1, and then randomly chose 40 of its satellites with $30 \leq r \leq 300$ kpc as observed tracers. Using the default prior on c , we calculate the joint probability distribution of $(\lg M, \lg c)$ from Equation (14) on a 2D grid. The best-fit values corresponding to the maximum likelihood, $(\lg M_{\text{esti}}, \lg c_{\text{esti}})$, are indicated by the red cross in Figure 4, where the 1σ and 2σ (68.3% and 95.4%) confidence contours are also shown in dark and faint red, respectively. For comparison, we replace the default prior on c with a flat prior and show the corresponding results in blue in Figure 4. From the marginalized distributions of $\lg M$ and $\lg c$ shown in the top and right panels, respectively, we obtain the statistical uncertainties, $\sigma_{\lg M} = 0.053$ (0.059) dex and $\sigma_{\lg c} = 0.087$ (0.14) dex, when the default (flat) prior on c is used. The default prior on c significantly reduces the uncertainty in the estimated $\lg c$ as expected, but it only slightly improves the precision of the estimated $\lg M$.

For both the default and flat priors on c , the best-fit value $\lg M_{\text{esti}}$ ($\lg c_{\text{esti}}$) is within $1\sigma_{\lg M}$ ($1\sigma_{\lg c}$) of the true value $\lg M_{\text{true}}$ ($\lg c_{\text{true}}$). As shown in Section 4.3, the $\sigma_{\lg M}$ and $\sigma_{\lg c}$ obtained in the above example application of our method to a single halo are reliable estimates of the statistical uncertainties, which dominate the total uncertainties when the number of observed tracers is < 100 .

Figure 5 shows the estimated density profile, $\rho(r)$, and mass distribution, $M(< r)$, for the default prior on c and compares them with their true counterparts. For either of these estimated functions, deviations from the true form are

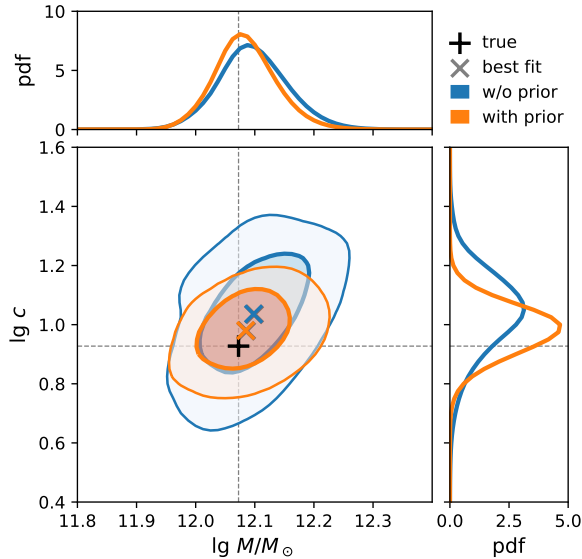


Figure 4. Estimated $\lg M$ and $\lg c$ from the kinematics of 40 tracers with $30 \leq r \leq 300$ kpc for a test halo. The results in red and blue are for the default and flat priors on c , respectively. The best-fit and true values are indicated by the cross and plus symbols, respectively. The dark and faint contours correspond to the 1σ and 2σ (68.3% and 95.4%) confidence levels. The top and right panels show the marginalized probability distributions for the estimated $\lg M$ and $\lg c$, respectively.

consistent with the estimated confidence levels. Specifically, $\rho(r)$ is tightly constrained at the $\sim 10\%$ level for most of the radial range of the observed tracers ($r \gtrsim 30$ kpc), and $M(< r)$ is best constrained at a similar level beyond the median radius, r_{med} , of the tracers. Similar results are found when the flat prior on c is used (not shown). Note that our method can provide tight constraints on $\rho(r)$ and $M(< r)$ throughout the outer halo. In contrast, the constraints reported by Wolf et al. (2010), Amorisco & Evans (2011), and Han et al. (2016c) quickly deteriorate away from a certain pinch point (usually near the half-mass radius or r_{med} , see Han et al. 2016c for a detailed discussion).

4.2. General performance

As shown by the example in Section 4.1, application of our method to a halo with a single set of observed tracers not only gives the best-fit values $\lg M_{\text{esti}}$ and $\lg c_{\text{esti}}$, but also the associated statistical uncertainties $\sigma_{\lg M}$ and $\sigma_{\lg c}$. A single application, however, cannot determine the systematic uncertainties. In this subsection, we estimate the total (systematic and statistical) uncertainties using the halo sample described in Section 3.1. We extend the analyses to separate the systematic from the statistical uncertainties in Section 4.3.

We apply our method to three sets of test halos, which differ in the number of tracers chosen for mock observations per

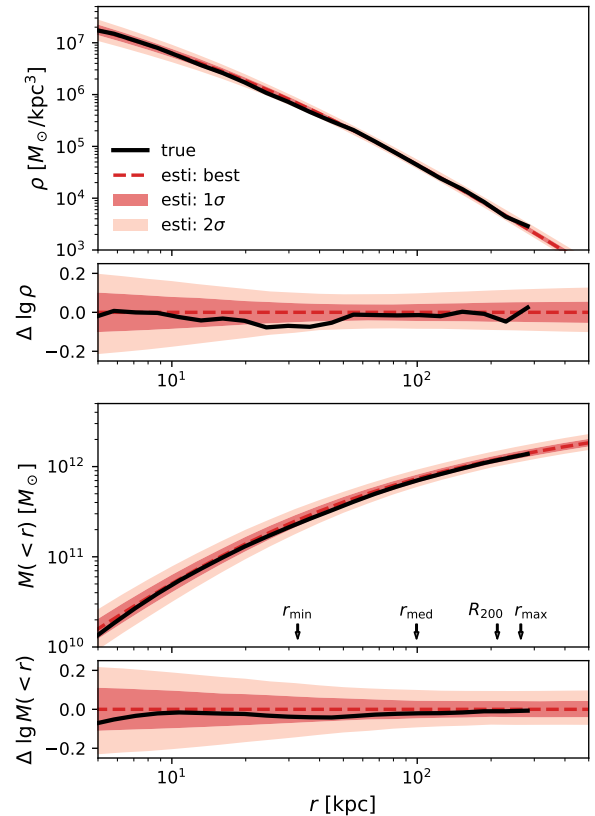


Figure 5. Comparison of the estimated $\rho(r)$ and $M(< r)$ (red) with their true counterparts (black) for the same test halo in Figure 4. The default prior on c is used. The dashed curves and dark (faint) shaded regions correspond to the best estimates and 1σ (2σ) confidence regions. The arrows indicate the minimum (r_{min}), median (r_{med}), and maximum (r_{max}) radii of the observed tracers, as well as the virial radius (R) of the halo.

halo. Specifically, the number of tracers used is $N_{\text{tracer}} = 10, 40, \text{ or } 80$, respectively. Clearly, for every halo in each set, the number of its satellites with $30 \leq r \leq 300$ kpc must exceed the corresponding N_{tracer} . As demonstrated in Appendix D, selection based on the richness of satellites for a halo does not introduce any bias. We apply our method to each test halo multiple times by randomly choosing different tracer subsamples. We include all the estimates obtained from this procedure so that a statistical result for each set of test halos is based on $\sim 10^4$ estimates.

The left panels of Figure 6 show the statistics on the deviations of the best-fit values, $\lg M_{\text{esti}}$ and $\lg c_{\text{esti}}$, from the true values, $\lg M_{\text{true}}$ and $\lg c_{\text{true}}$, respectively, for the three sets of test halos when the default or flat prior on c is used. It can be seen that our method provides asymptotically unbiased estimates, with better precision ($\sim 1/\sqrt{N_{\text{tracer}}}$) for a larger N_{tracer} . As quantitative measures of the total uncertainties, we use

$$\bar{\sigma}_{\text{tot}, \lg M} \equiv \sqrt{\text{var}(\lg M_{\text{esti}} - \lg M_{\text{true}})}, \quad (22)$$

$$\bar{\sigma}_{\text{tot}, \lg c} \equiv \sqrt{\text{var}(\lg c_{\text{esti}} - \lg c_{\text{true}})}, \quad (23)$$

where the variances are obtained from the corresponding distributions similar to those shown in the left panels of Figure 6. The filled (open) diamonds in the right panels of this figure show the $\bar{\sigma}_{\text{tot}, \lg M}$ and $\bar{\sigma}_{\text{tot}, \lg c}$ for $N_{\text{tracer}} = 10, 20, 40, 80,$ and 160 when the default (flat) prior on c is used. Similar to the example in Section 4.1, using the default prior on c can significantly improve the precision of the estimated $\lg c$ and mildly refine that of the estimated $\lg M$, especially when N_{tracer} is small. Note that the estimated $\lg M$ is approximately twice more precise than the estimated $\lg c$ for a flat prior on c . This result can be understood because in determining the depth of the potential as revealed by the tracers, the halo mass plays the primary role, whereas the concentration is only a secondary factor.

4.3. Systematic uncertainties

Whereas the basic assumptions of our method are reasonable and justified in Appendix B, deviations from them are expected when detailed aspects of the underlying cosmological simulation are considered. For example, the density profile of a halo may not be of the exact NFW type or not even strictly spherical. Some satellites may have been accreted as a group and stay correlated in phase space, so they cannot be treated as independent tracers following a general steady-state DF. Most importantly, variations in halo formation history may lead to different degrees of relaxation for satellite dynamics, and hence, varying deviations from a steady state. Such halo-to-halo scatter would violate strict scaling of internal dynamics for different halos. All deviations from our assumptions result in systematic uncertainties, which we estimate below by extending the analyses in Section 4.2.

For each test halo, we construct a corresponding stacked halo whose satellites follow our simulation-based DF exactly, and therefore, present no systematic uncertainties for our method. Let (r_s, v_s) be the characteristic scales for the test halo and (r'_s, v'_s) be those for another halo in the sample described in Section 3.1. We scale the (r', v') of every satellite for the latter halo to $(r = (r_s/r'_s)r', v = (v_s/v'_s)v')$. This procedure is repeated for all the halos other than the test halo in the above sample. The satellites for the test halo and those for all the scaled halos are assigned to the stacked halo. By construction, those satellites with $30 \leq r \leq 300$ kpc for this stacked halo exactly follow the DF in Equation (21) that applies to a halo having the same (M, c) as the test halo. Therefore, the estimated (M, c) for the stacked halo from our method only have statistical uncertainties.

Using the stacked halos corresponding to all the test halos in the sample described in Section 3.1, we perform similar analyses to those for the test halos as presented in Section 4.2. The statistical uncertainties in $\lg M$ and $\lg c$ obtained for the

stacked halos as functions of N_{tracer} for the default (flat) prior on c are shown as the thin gray solid (dashed) curves in the right panels of Figure 6. Note that because there are a large number of satellites for any stacked halo, we can extend the analyses to $N_{\text{tracer}} > 10^3$. Note also that the statistical uncertainties in $\lg M$ and $\lg c$ for the stacked halos become asymptotically independent of the prior on c for $N_{\text{tracer}} \gtrsim 100$ and 400, respectively.

For $N_{\text{tracer}} = 40$, the thin gray (solid or dashed) curves in the right panels of Figure 6 give $\bar{\sigma}_{\text{stats}} = 0.059$ (0.068) and 0.086 (0.18) for $\lg M$ and $\lg c$, respectively, when the default (flat) prior on c is used. These results are very close to those for the example application to a single halo presented in Section 4.1, which shows that the statistical uncertainties obtained from the Bayesian formalism of our method are reliable.

Taking the statistical uncertainties $\bar{\sigma}_{\text{stats}}$ in $\lg M$ and $\lg c$ for the test halos to be the same as those for the stacked halos shown as the thin gray (solid or dashed) curves in the right panels of Figure 6, we can estimate the systematic uncertainties $\bar{\sigma}_{\text{sys}}$ for the test halos by fitting

$$\bar{\sigma}_{\text{tot}}^2 = \bar{\sigma}_{\text{stats}}^2 + \bar{\sigma}_{\text{sys}}^2 \quad (24)$$

to the total uncertainties $\bar{\sigma}_{\text{tot}}$ shown as the (filled or open) diamonds in the right panels of the same figure for $N_{\text{tracer}} = 10, 20, 40, 80,$ and 160. We find that a good fit is obtained with $\bar{\sigma}_{\text{sys}} \approx 0.03$ (0.035) and 0.04 (0.07) dex for $\lg M$ and $\lg c$, respectively, when the default (flat) prior on c is used. Note that due to the lack of test halos with more than 160 satellites, we cannot obtain reliable estimates of the total uncertainties for $N_{\text{tracer}} > 160$. Using the above estimates for $\bar{\sigma}_{\text{stats}}$ and $\bar{\sigma}_{\text{sys}}$, however, we can calculate $\bar{\sigma}_{\text{tot}}$ for a wider range of N_{tracer} values. The results are shown as the thick black (solid or dashed) curves in the right panels of Figure 6. It can be seen that the statistical uncertainties $\bar{\sigma}_{\text{stats}}$ dominate for $N_{\text{tracer}} < 100$, whereas the systematic uncertainties $\bar{\sigma}_{\text{sys}}$ become non-negligible for $N_{\text{tracer}} \sim 100$ and dominate for $N_{\text{tracer}} \gtrsim 200$. Therefore, the optimal number of tracers for our method is $N_{\text{tracer}} \sim 100$. In general, the systematic uncertainties may be ignored for $N_{\text{tracer}} < 100$, especially when the observational errors are taken into account. Nevertheless, it is always useful to point out the intrinsic limitation of a method by providing the systematic uncertainties.

Here the systematic uncertainties are estimated based on a sample of isolated halos. A question arises when the MW is considered because its massive neighbor M31 is relatively close (~ 780 kpc). However, Li et al. (2017) showed that the influence of a massive neighbor on satellite kinematics of a host halo is small when the neighbor is at a distance exceeding 3 times its virial radius (see their Figure 13). Based on this criterion, M31 does not have a large effect on the kinematics of the MW satellites. So we expect that our method can be

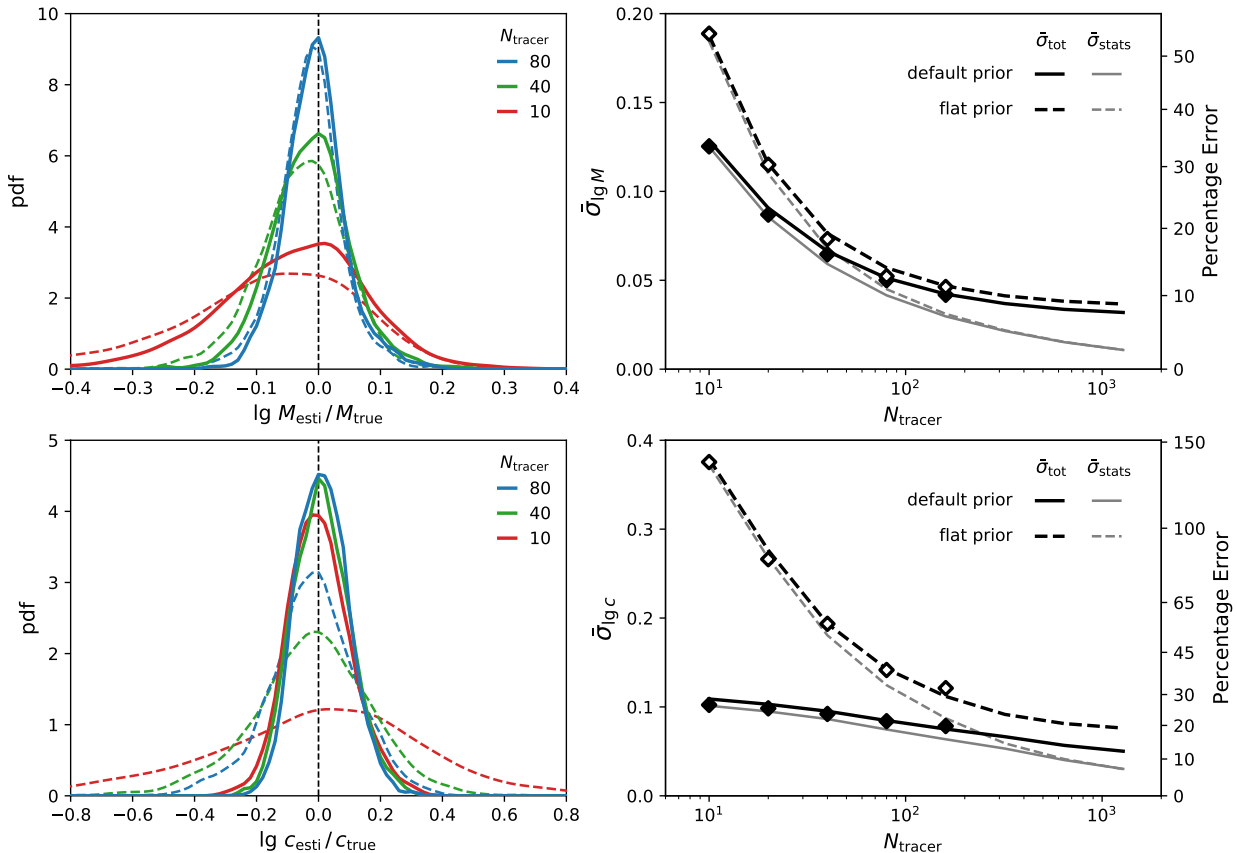


Figure 6. Precision of estimated $\lg M$ (upper panels) and $\lg c$ (lower panels) for the test halo sample. *Left panels:* Kernel smoothed distributions for the deviations of the best-fit values, $\lg M_{\text{esti}}$ and $\lg c_{\text{esti}}$, from the true values, $\lg M_{\text{true}}$ and $\lg c_{\text{true}}$, respectively. Results are shown for three sets of test halos, with a total of $N_{\text{tracer}} = 10, 40$, or 80 tracers, respectively, chosen for mock observations per halo. The solid (dashed) curves are for the default (flat) prior on c . *Right panels:* Uncertainties in the estimated $\lg M$ and $\lg c$ as functions of N_{tracer} . The diamonds show the total uncertainties calculated from the variances for similar distributions to those in the left panels. The thin gray curves show the statistical uncertainties estimated using the stacked halos. The differences between the diamonds and the corresponding gray curves give the estimated systematic uncertainties, which are combined with the estimated statistical uncertainties to give the total uncertainties shown as the thick black curves. The filled (open) diamonds and solid (dashed) curves are for the default (flat) prior on c .

applied to the MW with no large additional systematic uncertainties. Nevertheless, the systematic uncertainties of our method when applied to binary halos merit further detailed investigation.

4.4. Dependence on kinematic data

The above tests use the full set of kinematic data on the tracers as input. In view of the difficulty in obtaining accurate measurement of radial and tangential velocities, it is useful to study the dependence of the precision of our method on individual kinematic observables, thereby providing guidance on effective inclusion of tracers with incomplete data.

Using 40 tracers per halo with a flat prior on c , we apply our method to our test halo sample with data on (r, v_r, v_t) , (r, v_t) , and (r, v_r) , respectively (see Section 2.2.2 for the appropriate DF in the latter two cases). The resulting distributions of

$\lg(M_{\text{esti}}/M_{\text{true}})$ and $\lg(c_{\text{esti}}/c_{\text{true}})$ are shown in Figure 7. As expected, the data on (r, v_r, v_t) provide significantly more precise estimate of $\lg M$ than the data on either (r, v_t) or (r, v_r) . In addition, because v_t effectively represents two velocity components perpendicular to the radial direction, it provides tighter constraints on $\lg M$ than v_r . Note also that the estimated $\lg c$ is insensitive to which set of data among (r, v_r, v_t) , (r, v_t) , and (r, v_r) is used. We have also done tests with the data on r only (not shown), and find that spatial position provides very weak constraints compared with velocity. Therefore, with position only, a very large sample of tracers is required to provide meaningful estimates of halo properties.

As mentioned in Section 2.2.2, previous studies (e.g., Binney & Tremaine 2008; Wojtak et al. 2008) showed that the mass distribution of a system is mainly determined by the energy distribution of its constituents but is insensitive to their

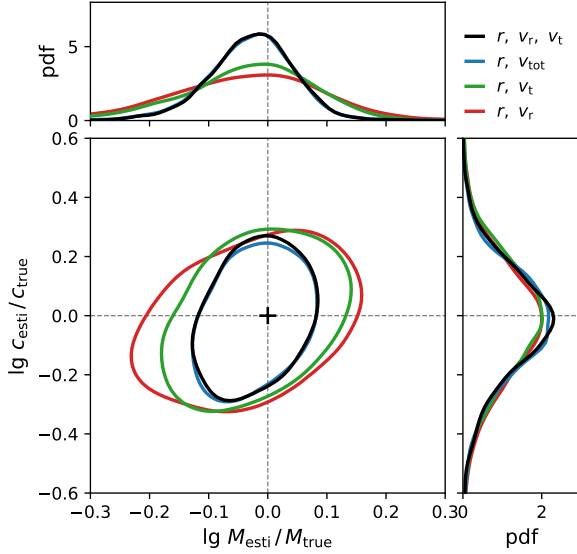


Figure 7. Tests of dependence of the precision on different sets of data for the halo sample. A total of 40 tracers per halo are used with a flat prior on c . The black, blue, green, and red curves show the 1σ confidence contours for the joint distribution of $\lg(M_{\text{esti}}/M_{\text{true}})$ and $\lg(c_{\text{esti}}/c_{\text{true}})$ from the data on (r, v_r, v_t) , (r, v_{tot}) , (r, v_t) , and (r, v_r) , respectively. The same color coding is used for the marginalized distributions of $\lg(M_{\text{esti}}/M_{\text{true}})$ and $\lg(c_{\text{esti}}/c_{\text{true}})$ shown in the top and right panels, respectively. Note that v_{tot} cannot be observed directly, but is calculated from v_r and v_t .

velocity anisotropy or angular momentum distribution. This result is supported by the work of Callingham et al. (2019), who found that using the probability density function in either the E or (E, L) space constrains the halo mass equally well. To further test the above result, we combine v_r and v_t into v_{tot} and apply our method using the data on (r, v_{tot}) (see Section 2.2.2 for the appropriate DF). The corresponding distributions of $\lg(M_{\text{esti}}/M_{\text{true}})$ and $\lg(c_{\text{esti}}/c_{\text{true}})$ are shown in Figure 7. It can be seen that the data on (r, v_{tot}) without distinguishing v_r and v_t provide essentially the same constraints on halo properties as the data on (r, v_r, v_t) . Therefore, whereas halo-to-halo scatter gives rise to systematic uncertainties of our method, the scatter in the velocity anisotropy contributes very little, which is consistent with the very small systematic uncertainties of our method. We note however, that v_{tot} cannot be measured directly. So although the influence of v_r and v_t enters our method mostly in the form of v_{tot} , this insensitivity to the velocity anisotropy only holds when both v_r and v_t are available. Otherwise, estimates of the halo mass are inevitably affected by the uncertainty in the velocity anisotropy (e.g., Wolf et al. 2010; Watkins et al. 2010).

4.5. Comparison with other methods

As mentioned in Section 1, many methods have been proposed to estimate the halo mass based on dynamical modeling, especially for the MW. Here we compare our method with the oPDF method⁴ (Han et al. 2016c). The oPDF method makes the minimum assumption of steady-state tracer dynamics in a static potential and is representative of a large category of steady-state methods, including those based on the Jeans equation and those based on the Jeans theorem such as Schwarzschild modeling. In turn, the Jeans equation method has been tested against many other methods and show close (or slightly better) precision compared to the caustic or virial method (e.g., Rines & Diaferio 2006; Old et al. 2015; Armitage et al. 2019).

Under the steady-state assumption, the oPDF method redistributes the radial position of each tracer along its orbit for a trial static potential according to $p(r|E, L)$ given by Equation (6). The difference between the resulting radial distribution of the tracer sample and the observed distribution is minimized using a likelihood function to infer the correct potential. In principle, the oPDF method can be applied to potentials of arbitrary (including non-spherical) form. In the comparison below, we take the potential of a test halo as given by its fitted NFW profile and use the radial likelihood estimator of the oPDF method (with 10 radial bins, see Han et al. 2016c for details) to infer the corresponding halo mass and concentration.

In addition, to further illustrate the difference between our method, which is based on the DF, $f(E, L)$, in the phase space of (\mathbf{r}, \mathbf{v}) , and the method of Li et al. (2017) (see also Callingham et al. 2019), which is based on the probability density function, $p(E, L)$, in the (E, L) space, we compare these two methods using the self-consistent $f(E, L)$ and $p(E, L)$ of our method. Note that our $p(E, L)$ can be used to infer both the halo mass and concentration, whereas the method of Li et al. (2017) was developed for estimating the halo mass only. To mimic that method more closely, we also apply it assuming the average $\lg M - \lg c$ relation for our halo sample (see Equation 19) so that only the halo mass needs to be inferred.

Using 80 tracers per halo with a flat prior on c (except for the $p(E, L)$ method with the average $\lg M - \lg c$ relation), we apply the above methods to our halo sample and show their distributions of $\lg(M_{\text{esti}}/M_{\text{true}})$ and $\lg(c_{\text{esti}}/c_{\text{true}})$ in Figure 8 and give the corresponding average values, $\langle \lg(M_{\text{esti}}/M_{\text{true}}) \rangle$ and $\langle \lg(c_{\text{esti}}/c_{\text{true}}) \rangle$, as well as the total uncertainties, $\bar{\sigma}_{\lg M}$ and $\bar{\sigma}_{\lg c}$, in Table 1. It can be seen that both the oPDF method and our method are able to provide unbiased estimates of the halo mass and concentration. Note that although the distribution of $\lg(M_{\text{esti}}/M_{\text{true}})$ for the oPDF method sharply

⁴ The Python implementation of the oPDF method is publicly available at <https://github.com/Kambrian/oPDF>.

peaks at zero, its long tails on both sides of the peak result in a larger total uncertainty than that for our method. The oPDF method is also less precise in estimating $\lg c$ than our method, although the precision can be improved in both cases when the default prior on c is used (not shown). A similar comparison with similar results to the above was shown in Figure 3 of Han et al. (2016c) for an idealized case.

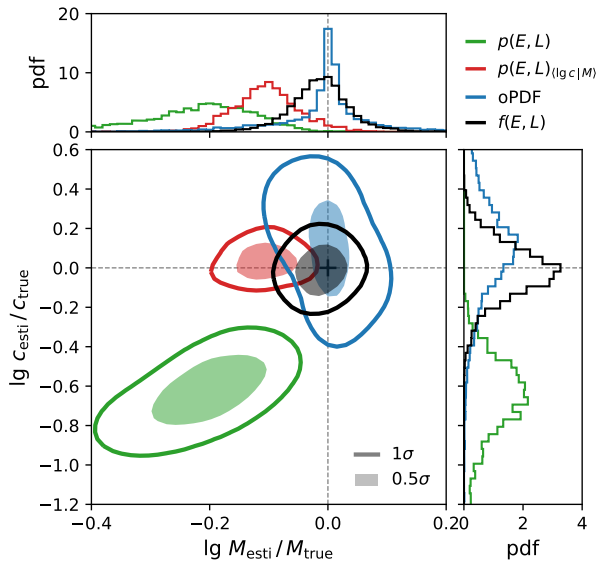


Figure 8. Comparison of different methods applied to the halo sample with 80 tracers per halo. A flat prior on c is used except for the method based on $p(E, L)$ with the average $\lg M$ – $\lg c$ relation (labeled $p(E, L)_{\langle \lg c | M \rangle}$). The black, blue, green, and red curves (shaded areas) show the 1σ (0.5σ) confidence contours (regions) for the joint distribution of $\lg(M_{\text{esti}}/M_{\text{true}})$ and $\lg(c_{\text{esti}}/c_{\text{true}})$ for our method (labeled $f(E, L)$), the oPDF method, the method based on $p(E, L)$, and the method based on $p(E, L)_{\langle \lg c | M \rangle}$, respectively. The same color coding is used for the marginalized distributions of $\lg(M_{\text{esti}}/M_{\text{true}})$ and $\lg(c_{\text{esti}}/c_{\text{true}})$ shown in the top and right panels, respectively.

Table 1. Comparison of the methods as shown in Figure 8.

	$\langle \lg \frac{M_{\text{esti}}}{M_{\text{true}}} \rangle$	$\sigma_{\lg M}$	$\langle \lg \frac{c_{\text{esti}}}{c_{\text{true}}} \rangle$	$\sigma_{\lg c}$
$p(E, L)$	-0.24	0.13	-0.68	0.23
$p(E, L)_{\langle \lg c M \rangle}$	-0.10	0.06	–	–
oPDF	-0.00	0.11	0.14	0.41
$f(E, L)$	-0.01	0.05	-0.02	0.14

As already noted by Li et al. (2017), the estimated halo mass based on $p(E, L)$ has an intrinsic bias. We have mentioned in Section 1 that this bias arises because E is not directly observed. For estimating halo properties based on the (\mathbf{r}, \mathbf{v}) of tracers, the proper DF to use is $f(E, L)$. With

$p(E, L) = 8\pi^2 L T_r(E, L) f(E, L)$, a potential with a longer radial orbital period $T_r(E, L)$ for the same (\mathbf{r}, \mathbf{v}) is favored by $p(E, L)$. Because a shallower potential corresponding to a lower halo mass allows a tracer to have a more distant apocenter, and hence, a longer $T_r(E, L)$, the method based on $p(E, L)$ underestimates the halo mass. Figure 8 and Table 1 indeed show such a bias. Note that both the bias and the total uncertainty for the estimated halo mass are reduced significantly when the average $\lg M$ – $\lg c$ relation is used in the method based on $p(E, L)$ to mimic the original method of Li et al. (2017). The typical bias of ~ -0.1 dex in this case is also consistent with the results of Li et al. (2017).

Although the method based on $p(E, L)$ gives biased estimates of the halo mass, it qualitatively illustrates the constraining power of the orbital distribution in the (E, L) space, whereas the oPDF method shows that of the radial distribution $p(r|E, L)$ along each orbit. As indicated by the nearly orthogonal 1σ confidence contours of these two methods in Figure 8, the tightest constraints on halo properties are provided by combining both the orbital distribution and the radial distribution along each orbit, which is exactly done by the DF, $f(E, L)$, of our method (see Equation 5). Therefore, our method is more precise than the oPDF method as shown above, and perhaps, has the best performance among the currently existing methods.

5. APPLICATIONS TO THE MW AND BEYOND

A key motivation for this work is to estimate the mass and its detailed distribution for the MW halo. These properties are crucial to many astrophysical studies, but remain rather uncertain (see Wang et al. 2019 in preparation for a comprehensive summary of recent measurements). Whereas satellite galaxies are the best tracers for the mass distribution of the outer MW halo and the total halo mass (Han et al. 2019), their use for mass estimates has been limited by their small sample size and poor kinematic data until recently. Deep sky surveys have doubled the number of known MW satellites over the past several years (see Simon 2019 for a review). In addition, the unprecedented precision of Gaia (Gaia Collaboration et al. 2018a) has enabled better proper motion measurement for the MW satellites (e.g., Gaia Collaboration et al. 2018b; Kallivayalil et al. 2018; Pace & Li 2019; Fritz et al. 2018). With the above improvements of the data, we apply our method to the MW. The details are presented in a separate paper (Li et al. 2019, in preparation), and the main results are summarized below.

Using 28 satellites with Gaia DR2 proper motion data and the DF model based on halos in the Eagle simulation, we obtain $M = 1.23^{+0.21}_{-0.18} \times 10^{12} M_{\odot}$ and $c = 9.4^{+2.8}_{-2.1}$ for the MW halo. Both the selection function and measurement errors are taken into account and treated rigorously within the Bayesian

statistical framework of our method. With a $\sim 20\%$ uncertainty, our estimated MW halo mass is currently the most precise. The systematic error due to halo-to-halo scatter is small compared to the current statistical uncertainty. The inferred halo mass is consistent with recent measurements using satellites (Li et al. 2017; Callingham et al. 2019; Patel et al. 2018), stars (e.g., Zhai et al. 2018; Deason et al. 2019), and globular clusters (e.g., Sohn et al. 2018; Watkins et al. 2019; Vasiliev 2019). This mass estimate can be further improved if multiple tracer populations (e.g., satellites and halo stars) are used in combination (Li et al. 2019, in preparation). In addition, our DF model along with the estimated halo mass can be used to constrain the kinematics of distant satellites, so that their orbits, and hence the assembly history of the MW, may be better inferred.

In principle, our method can be applied to halos of any mass or concentration, including galaxy groups or clusters, so long as these systems follow the same DF when scaled by the corresponding r_s and v_s . Galaxy clusters, however, are further from equilibrium compared to galactic halos. The larger halo-to-halo scatter for the former is expected to result in a larger intrinsic uncertainty. In addition, substructures in more massive halos tend to move along more radial orbits. This feature may be problematic when there are no data on the associated proper motion. As discussed in Section 4.4, although our method is insensitive to the velocity anisotropy when the full kinematic information of the tracers is available, lack of either v_r or v_t is expected to weaken this insensitivity, thereby increasing the intrinsic uncertainty due to the halo-to-halo scatter from the velocity anisotropy. In practice, the above issues can be mitigated by constructing the appropriate DF from template halos in the relevant mass range.

For application to distant galaxies, we must deal with more complex observations (e.g., Biviano et al. 2006; Wojtak et al. 2018; Lange et al. 2019; Pratt et al. 2019). For example, when only the projected position and line-of-sight velocity are observed for satellites, we need to marginalize the DF to model the projected phase space (see e.g., Dejonghe & Merritt 1992). In addition, there are other problems common to nearly all methods, such as foreground and background contamination (interlopers), incompleteness (e.g., caused by fiber collision), mis-centering, modeling of the infall region near the halo boundary, and influence of the large-scale structure. All of the above issues require careful treatment and merit future studies.

6. DISCUSSION AND CONCLUSIONS

We have proposed a new method to estimate the properties, especially the mass, of a halo from the phase-space distribution of its satellites. The DF in phase space is constructed directly from a cosmological simulation assuming similarity

of internal dynamics for different halos. Within the fully Bayesian framework of our method, which is unbiased and efficient, we are able to infer both the halo mass and the concentration, and treat various observational effects, including the selection function, incomplete data (e.g., lack of proper motion), and observational errors (see Li et al. 2019, in preparation) in a rigorous manner.

We have tested the validity and accuracy of our method with mock samples. Making full use of the DF in phase space, our method achieves better precision than the oPDF method, which is representative of a large family of pure steady-state methods, including those based on the Jeans equation and Schwarzschild modeling. Because our new method makes use of the mass-dependent distribution of orbits in addition to the steady-state distribution along each orbit, we are able to slightly reduce the stochastic systematic uncertainty (Wang et al. 2017, 2018) that represents the information limit of pure steady-state methods. In the ideal case without observational errors, we are able to constrain the halo mass at the 20% level (~ 0.08 dex in $\lg M$) with only 20 satellites. The systematic uncertainty is $\sim 8\%$ (~ 0.035 dex in $\lg M$) for the halo mass and $\sim 16\%$ (~ 0.07 dex in $\lg c$) for the concentration with a flat prior on the latter.

These results are comparable to the $\sim 25\%$ and 40% systematic uncertainties⁵ found in Wang et al. (2017, 2018) for the halo mass and concentration, respectively, when dark matter particles from simulations were used as tracers. On the other hand, the systematic uncertainties when using star particles as tracers can be as high as $\sim 300\%$ according to Wang et al. (2017, 2018), much larger than what we found using satellite tracers. These results can be understood as satellite galaxies are nearly unbiased phase-space tracers of dark matter particles, while halo stars remain highly phase-correlated after getting stripped from their progenitors. We leave more detailed comparisons and discussions of the different tracers to a separate paper (Han et al. 2019).

A major application of our method is to estimate the MW halo mass. Using the kinematic data of satellites updated by Gaia, we obtain a mass of $1.23 \times 10^{12} M_\odot$ with a $\sim 20\%$ uncertainty for the MW halo, which is consistent with other recent estimates from various tracers (e.g., Callingham et al. 2019; Patel et al. 2018; Deason et al. 2019; Zhai et al. 2018; Sohn et al. 2018; Watkins et al. 2019; Vasiliev 2019). The significantly lower mass $M = 0.71 \times 10^{12} M_\odot$ obtained by Eadie & Jurić (2019) likely reflects the specific assumptions in the underlying DF model and gravitational potential. A detailed

⁵ There is a subtle difference between the systematic uncertainties quoted in Wang et al. (2017, 2018) and ours. The former uncertainty was based on the extent of the 1σ confidence region in the two-dimensional (M, c) space, while we adopt the marginalized one-dimensional uncertainty which is expected to be about half of the corresponding two-dimensional extent.

report is given elsewhere (Li et al. 2019, in preparation). Our method can also be applied to other halos including galaxy groups or clusters. We plan to carry out such followup studies in the future.

We have used a mock galaxy sample, which was generated from the SAM based on a cosmological simulation, to construct the DF and validate our method. Whereas the validity of our method has been demonstrated for this SAM sample, whether this sample represents actual galaxies is a concern when we apply our method to the MW and other real systems. Simulations and models of galaxy formation are plagued by the poorly-understood processes in baryon-dominated regions. In general, the presence of a stellar disc and adiabatic contraction of a halo would alter the potential of the inner halo and enhance the tidal disruption of substructures. Simulations, however, show that satellites in the outer halo are less affected (e.g., Zhu et al. 2016; Sawala et al. 2017; Richings et al. 2018). In particular, satellite kinematics is largely unchanged by baryonic physics for radii exceeding one quarter of the virial radius (Sawala et al. 2017; Richings et al. 2018). In addition, Gifford et al. (2013) reported that halo mass estimates using satellites are insensitive to variation of the dynamical friction applied to the “orphan” galaxies in the SAM. Therefore, the SAM galaxy sample provides a reasonable means to represent the satellite kinematics in the outer halos of real galaxies, and our method can be used to estimate the properties of these systems from the actual satellite data. Nevertheless, the appropriateness of the SAM galaxy sample warrants more in-depth and systematic studies. More detailed comparison of halo mass estimates based on SAM and hydrodynamic simulations will be given in Li et al. 2019, in preparation.

Finally, the validity of our method supports the similarity of internal dynamics of different halos, at least for the SAM galaxy sample. The corresponding DF can provide some insights into and facilitate analytical studies of the dynamical state of halos.

We thank Radosław Wojtak for communications on DF models, and Carlos S. Frenk, Lu Li, Ting Li, Zhengyi Shao, and Jiajun Zhang for helpful discussions. This work was supported in part by the National Natural Science Foundation of China [11533006, 11621303, 11890691, 11655002, 11873038], National Key Basic Research and Development Program of China (No. 2018YFA0404504), the US Department of Energy [DE-FG02-87ER40328 (UM)], the National Program on Key Basic Research Project (Grant No. 2015CB857003), the Science and Technology Commission of Shanghai Municipality [16DZ2260200], and JSPS Grant-in-Aid for Scientific Research JP17K14271.

This work made use of the High Performance Computing Resource in the Core Facility for Advanced Research Computing at Shanghai Astronomical Observatory, and the computing facilities at Department of Astronomy, School of Physics and Astronomy, Shanghai Jiao Tong University.

Software: Numpy (van der Walt et al. 2011), Scipy (Oliphant 2007), Matplotlib (Hunter 2007), Astropy (Astropy Collaboration et al. 2013), oPDF (Han et al. 2016c)

APPENDIX

A. RELATION BETWEEN PHASE SPACE AND (E, L) SPACE

Here we derive the relation between the DF $f(E, L)$ in the phase space of (\mathbf{r}, \mathbf{v}) and the probability density function $p(E, L)$ in the (E, L) space. From the assumed spherical symmetry, we can write

$$f(\mathbf{r}, \mathbf{v})d^3\mathbf{r}d^3\mathbf{v} = f(r, v_r, v_t)8\pi^2r^2v_t dr dv_r dv_t. \quad (\text{A1})$$

Because we can fully specify a tracer by the (E, L) of its orbit and its radius, r , we have

$$f(r, v_r, v_t)8\pi^2r^2v_t dr dv_r dv_t = p(r|E, L)p(E, L)dr dE dL, \quad (\text{A2})$$

where $p(r|E, L)$ is the probability density function of r for a specific set of (E, L) . Using the Jacobian for the transformation of variables from (r, E, L) to (r, v_r, v_t) ,

$$\frac{\partial(r, E, L)}{\partial(r, v_r, v_t)} = r|v_r|, \quad (\text{A3})$$

we rewrite Equation (A2) as

$$f(r, v_r, v_t) = \frac{|v_r|}{8\pi^2L}p(r|E, L)p(E, L), \quad (\text{A4})$$

which is Equation (5) in Section 2.

It is useful to define a radial phase angle

$$\theta \equiv \frac{2\pi}{T_r(E, L)} \int_{r_{\text{peri}}}^r \frac{dr'}{v_r(r', E, L)}, \quad (\text{A5})$$

where

$$v_r(r', E, L) = \pm\sqrt{2[E - \Phi(r')] - L^2/r'^2}, \quad (\text{A6})$$

and the plus (minus) sign is for motion away from (towards) the pericenter. Equation (6) can now be rewritten as

$$p(r|E, L)dr = p(\theta|E, L)d\theta = \frac{d\theta}{2\pi}. \quad (\text{A7})$$

Thus, θ is uniformly distributed over $[-\pi, \pi]$ under our steady-state assumption.

Note that when a sample of satellites with a limited radial range of $r_{\min} \leq r \leq r_{\max}$ is used to construct $f(E, L)$, the lower and upper limits for the radial integral in Equation (7) for $T_r(E, L)$ should be replaced by $\max\{r_{\text{peri}}, r_{\min}\}$ and $\min\{r_{\text{apo}}, r_{\max}\}$, respectively (Wojtak et al. 2008). Similar adjustments should be made for θ as well. Nevertheless, it is important to recognize that the DF $f(E, L)$ is not subject to any radial limit. As the radial range changes, both $p(E, L)$ and $p(r|E, L)$ vary in a complementary way to keep their product invariant, so long as the entire system is in a steady state.

B. VALIDITY OF ASSUMPTIONS

Our assumed NFW profile for halos is a well-known result in the framework of hierarchical structure formation (Navarro et al. 1996). This profile is a good fit for our halo sample, with differences of $\lesssim 3\%$ between the fitted halo masses and the true values.

As a check on the assumed steady state of satellite kinematics, we show that satellites in our template sample are uniformly distributed in phase angles along the orbits (see e.g., Binney & Tremaine 2008; Han et al. 2016c). In other words, the probability density function $p(\theta|E, L)$ is $1/(2\pi)$ as in Equation (A7). Note that satellites in our template sample have $r < r_{\text{lim}} = 25r_s$. So the upper limit for the radial integral in Equation (7) for $T_r(E, L)$, as well as the maximum r for the definition of θ in Equation (A5), should be the smaller of r_{lim} and r_{apo} .

It is difficult to show $p(\theta|E, L)$ directly, which requires 4D display. Instead, we show in Figure 9 the distribution $\tilde{p}(\theta) = \int \tilde{p}(\theta|\tilde{E}, \tilde{L})\tilde{p}(\tilde{E}, \tilde{L})d\tilde{E}d\tilde{L}$, and the average value $\langle\theta(\tilde{E}, \tilde{L})\rangle = \int \theta\tilde{p}(\theta|\tilde{E}, \tilde{L})d\theta$ as a function of (\tilde{E}, \tilde{L}) , for the satellites in our template sample. It can be seen that $\tilde{p}(\theta) \approx 1/(2\pi)$ and $\langle\theta(\tilde{E}, \tilde{L})\rangle \approx 0$ for all sets of (\tilde{E}, \tilde{L}) , as expected from $\tilde{p}(\theta|\tilde{E}, \tilde{L}) = 1/(2\pi)$. In addition, we show in Figure 9 numbers of satellites in various $(\tilde{\theta}, \tilde{E})$ or $(\tilde{\theta}, \tilde{L})$ bins, which are also in excellent agreement with a uniform distribution of θ .

Finally, our assumption regarding the similarity of internal dynamics for different halos is supported by the results of Li et al. (2017) and Callingham et al. (2019) on the probability density function $\tilde{p}(\tilde{E}, \tilde{L})$ in the (\tilde{E}, \tilde{L}) space. In addition, we show in Figure 10 the distributions $\tilde{f}(\tilde{E}, \tilde{L})$ in the phase space of (\tilde{r}, \tilde{v}) that are constructed from our template sample of satellites and its subsamples for halos with $\lg M/M_\odot \in [11.5, 12.5]$, $[11.5, 11.8]$, and $[12.45, 12.5]$, respectively. It can be seen that all these distributions are nearly identical despite the large differences in the halo mass range used.

C. DETAILS OF CONSTRUCTING THE DF

We use the satellites in the template sample to construct a smooth DF in the phase space of (\tilde{r}, \tilde{v}) . All the satellites have $\tilde{r} \leq \tilde{r}_{\text{lim}} = 25$ relative to the centers of their host ha-

los. Because their (\tilde{E}, \tilde{L}) are unevenly distributed in a sharp triangular region (see e.g., Li et al. 2017), a fixed smoothing kernel in the (\tilde{E}, \tilde{L}) space is not adequate. Instead, an adaptive smoothing procedure is needed. We perform this procedure in the parameter space of (\tilde{E}, j^2) , where $j = \tilde{L}/\tilde{L}_{\text{max}}(\tilde{E}) \in [0, 1]$ and $\tilde{L}_{\text{max}}(\tilde{E})$ is the maximum angular momentum for a satellite of energy \tilde{E} in the template sample. If the radius of the circular orbit for the energy \tilde{E} is $\tilde{r}_{\text{cir}}(\tilde{E}) \leq \tilde{r}_{\text{lim}}$, then $\tilde{L}_{\text{max}}(\tilde{E})$ is the angular momentum of the circular orbit, $\tilde{L}_{\text{cir}}(\tilde{E})$, and j is the so-called orbital circularity. Clearly, this definition of $\tilde{L}_{\text{max}}(\tilde{E})$ does not apply if $\tilde{r}_{\text{cir}} > \tilde{r}_{\text{lim}}$ or if the orbit is unbound with $\tilde{E} > \tilde{\Phi}(\infty) = 1$. For these two cases, we define $\tilde{L}_{\text{max}}(\tilde{E})$ as the product of \tilde{r}_{lim} and the total velocity \tilde{v}_{tot} at this radius for the energy \tilde{E} , so that $j \in [0, 1]$ is again valid. Specifically, we have

$$\tilde{L}_{\text{max}}(\tilde{E}) = \begin{cases} \tilde{L}_{\text{cir}}(\tilde{E}), & \text{for } \tilde{r}_{\text{cir}}(\tilde{E}) \leq \tilde{r}_{\text{lim}}, \\ \tilde{r}_{\text{lim}}\sqrt{2[\tilde{E} - \tilde{\Phi}(\tilde{r}_{\text{lim}})]}, & \text{otherwise,} \end{cases} \quad (\text{C8})$$

which is shown as the dot-dashed curve in Figure 9b.

The DF in Equation (8) can be rewritten as

$$\tilde{f}(\tilde{E}, \tilde{L}) = \frac{1}{4\pi^2\tilde{T}_r(\tilde{E}, \tilde{L})\tilde{L}_{\text{max}}^2(\tilde{E})} \times \frac{d^2N}{d\tilde{E}dj^2}. \quad (\text{C9})$$

To obtain a smooth $\tilde{f}(\tilde{E}, \tilde{L})$, we construct a smooth $d^2N/d\tilde{E}dj^2$ with adaptive kernel density estimation as follows:

$$\frac{d^2N}{d\tilde{E}dj^2} = \frac{1}{N_h} \sum_{i=1}^{N_h} \frac{1}{N_{s,i}} \sum_{k=1}^{N_{s,i}} \mathcal{S}(\tilde{E} - \tilde{E}_{ik}, \sigma_{\tilde{E}}) \mathcal{S}(j^2 - j_{ik}^2, \sigma_{j^2}), \quad (\text{C10})$$

where N_h is the total number of halos in the template sample, $N_{s,i}$ is the total number of satellites in the i th halo, $(\tilde{E}_{ik}, j_{ik}^2)$ refer to the k th satellite of the i th halo, and the sums run over every satellite in every halo. In Equation (C10), \mathcal{S} denotes the Gaussian smoothing kernel, and the kernel sizes are chosen adaptively as $\sigma_{\tilde{E}} = 15\epsilon_{\text{sep}}$ and $\sigma_{j^2} = 24\epsilon_{\text{sep}}$, where the difference between the numerical factors corresponds to that between the standard deviations of \tilde{E} and j^2 for satellites in the template sample, and ϵ_{sep} is the local average particle separation as used for smoothed particle hydrodynamics.⁶ In the above smoothing procedure, reflecting boundary is used at $\tilde{E} = 0$, as well as at $j^2 = 0$ and 1.

As shown in Figure 9b, the satellites in our template sample do not cover the upper right corner of the (\tilde{E}, \tilde{L}) space that lies above the dot-dashed curve and to the right

⁶ We estimate the local average separation for a target particle as $\epsilon_{\text{sep}} = d_n\sqrt{\pi/n}$, where d_n is the distance to the n th nearest neighbor (see e.g., Price 2012). We take $n = 50$, but ϵ_{sep} is not sensitive to n and typically ranges from ≈ 0.02 to ≈ 0.2 for the satellites in our template sample.

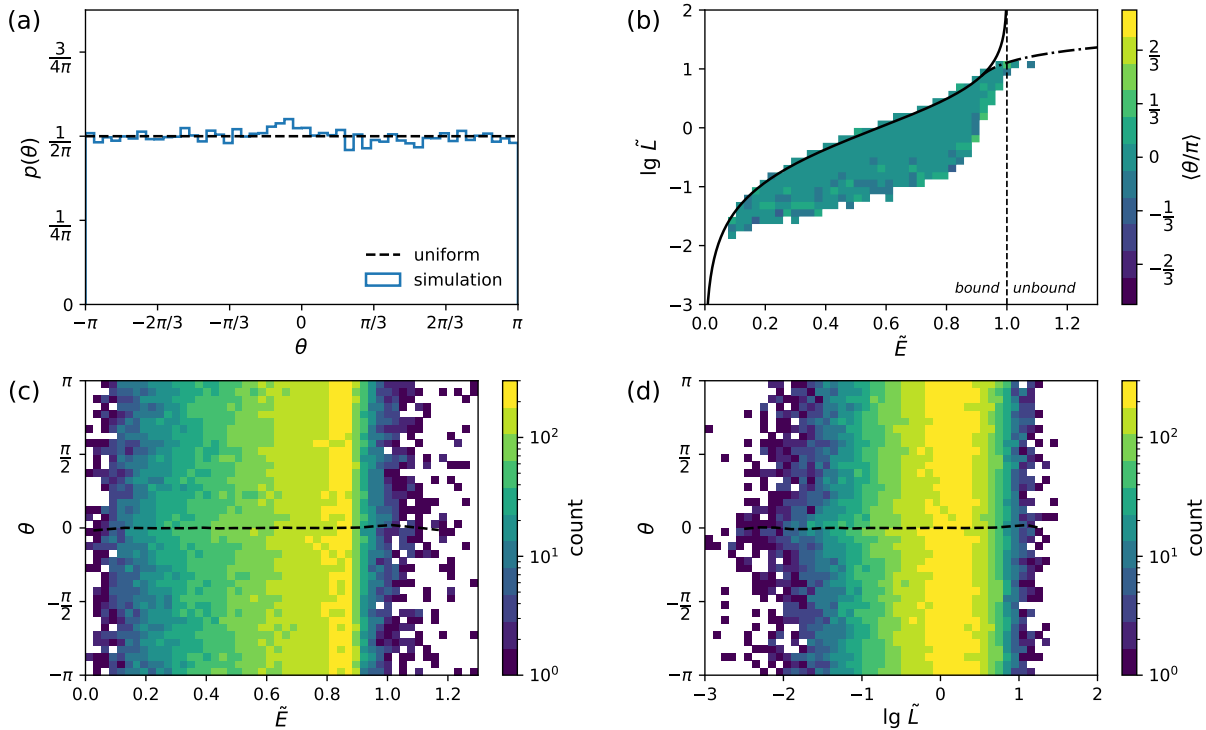


Figure 9. Distributions of radial phase angle θ for satellites in the template sample. (a) The distribution $\tilde{p}(\theta) = \int \tilde{p}(\theta|\tilde{E}, \tilde{L})\tilde{p}(\tilde{E}, \tilde{L})d\tilde{E}d\tilde{L}$. (b) The average value $\langle \theta(\tilde{E}, \tilde{L}) \rangle = \int \theta \tilde{p}(\theta|\tilde{E}, \tilde{L})d\theta$ as a function of $(\tilde{E}, \tilde{L}) = (E/v_s^2, L/(rv_s))$. Only pixels with more than 20 satellites are displayed. The solid (dot-dashed) curve shows the maximum \tilde{L} as a function of \tilde{E} for any radius (for $r < 25r_s$). (c) Numbers of satellites in various (θ, \tilde{E}) bins. (d) Numbers of satellites in various (θ, \tilde{L}) bins. The dashed curve in (c) or (d) shows the average θ for bins with a fixed \tilde{E} or \tilde{L} , respectively.

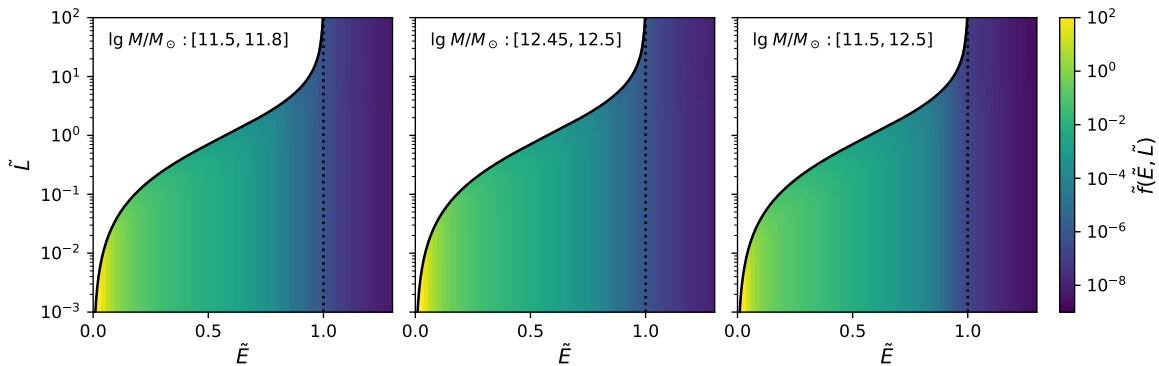


Figure 10. Phase-space distribution functions $\tilde{f}(\tilde{E}, \tilde{L})$ constructed from the template sample of satellites and its subsamples for halos in the indicated mass ranges. The left or middle panel contains $\approx 10^4$ satellites. The right panel is for the template sample of 104,315 satellites and is the same as the DF shown in Figure 3.

of the solid curve. Because this region is physically accessible, we estimate the corresponding $\tilde{f}(\tilde{E}, \tilde{L})$ as follows. We note that the solid and dot-dashed curves in Figure 9b start to diverge at $(\tilde{E}_{\text{lim}}, \tilde{L}_{\text{lim}})$, where \tilde{E}_{lim} corresponds to $\tilde{r}_{\text{cir}}(\tilde{E}_{\text{lim}}) = \tilde{r}_{\text{lim}}$ and $\tilde{L}_{\text{lim}} = \tilde{L}_{\text{cir}}(\tilde{E}_{\text{lim}})$. For simplicity, we take $\tilde{f}(\tilde{E}, \tilde{L}) = \tilde{f}(\tilde{E}, \tilde{L}_{\text{lim}})$ for the region of (\tilde{E}, \tilde{L}) that lies above $\tilde{L} = \tilde{L}_{\text{lim}}$ and to the right of the solid curve in Figure 9b. This estimate is partly based on continuity of $\tilde{f}(\tilde{E}, \tilde{L})$.

It also follows from the assumption that unbound or nearly unbound satellites have an isotropic DF with dependence on \tilde{E} only. This assumption seems reasonable because high-speed satellites are mainly accelerated by the external field, so their direction of motion is largely unrelated to the host halo. In any case, because most satellites are sufficiently bound to their host halos, our method of estimating the halo mass is

not sensitive to the $\tilde{f}(\tilde{E}, \tilde{L})$ adopted for the region of (\tilde{E}, \tilde{L}) discussed above.

D. VALIDITY AND ROBUSTNESS OF THE METHOD

Using 20 tracers per halo with a flat prior on c , we check the validity and robustness of our method by applying it to halos in the sample described in Section 3.1. Specifically, we test if the precision of the estimated $\lg M$ depends on the halo mass, the concentration, the richness of satellites, and the largest satellite mass at infall, respectively. The last factor is motivated by the potential influence of the Large Magellanic Cloud on the mass estimate of the MW halo. We calculate $\lg(M_{\text{esti}}/M_{\text{true}})$ for test halos in the whole pertinent sample, and for those in the top and bottom 20% of this sample, respectively, based on each of the above factors. The corresponding distributions are shown in Figure 11. It can be seen that the precision of the estimated $\lg M$ does not depend on any of the above factors.

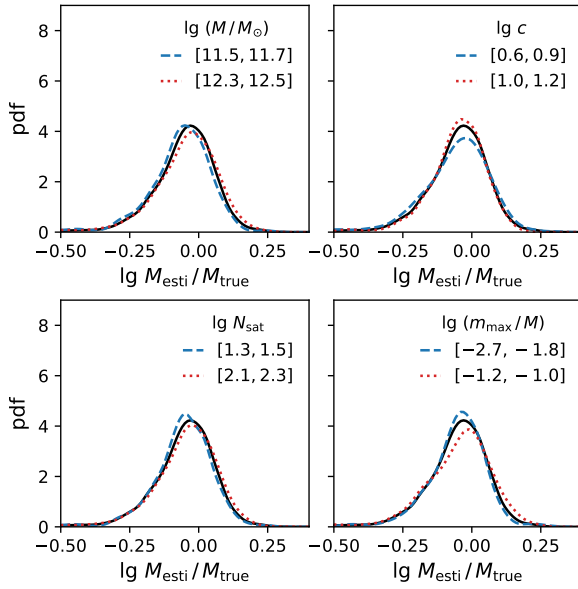


Figure 11. Tests of dependence of the precision on various factors. *Upper left panel:* Halo mass, M . *Upper right panel:* Halo concentration, c . *Lower left panel:* Number of satellites, N_{sat} . *Lower right panel:* Ratio of the largest satellite mass at infall, m_{max} , to the halo mass. The black solid curve is the same for all panels and shows the distribution of $\lg(M_{\text{esti}}/M_{\text{true}})$ for test halos in the whole pertinent sample, whereas the red dotted (blue dashed) curves show the distributions for those in the top (bottom) 20% of this sample with the indicated range of the relevant factor.

REFERENCES

Amorisco, N. C., & Evans, N. W. 2011, *MNRAS*, **411**, 2118

- Armitage, T. J., Kay, S. T., Barnes, D. J., Bahé, Y. M., & Dalla Vecchia, C. 2019, *MNRAS*, **482**, 3308
- Astropy Collaboration, Robitaille, T. P., Tollerud, E. J., et al. 2013, *A&A*, **558**, A33
- Binney, J., & Tremaine, S. 2008, *Galactic Dynamics: Second Edition*
- Biviano, A., Murante, G., Borgani, S., et al. 2006, *A&A*, **456**, 23
- Boylan-Kolchin, M., Springel, V., White, S. D. M., Jenkins, A., & Lemson, G. 2009, *MNRAS*, **398**, 1150
- Callingham, T. M., Cautun, M., Deason, A. J., et al. 2019, *MNRAS*, **484**, 5453
- Courteau, S., Cappellari, M., de Jong, R. S., et al. 2014, *RvMP*, **86**, 47
- Deason, A. J., Fattahi, A., Belokurov, V., et al. 2019, *MNRAS*, **485**, 3514
- Dejonghe, H., & Merritt, D. 1992, *ApJ*, **391**, 531
- Diaferio, A., & Geller, M. J. 1997, *ApJ*, **481**, 633
- Dutton, A. A., & Macciò, A. V. 2014, *MNRAS*, **441**, 3359
- Eadie, G., & Jurić, M. 2019, *ApJ*, **875**, 159
- Eadie, G. M., Harris, W. E., & Widrow, L. M. 2015, *ApJ*, **806**, 54
- Evans, N. W., & An, J. H. 2006, *PhRvD*, **73**, 023524
- Evans, N. W., Wilkinson, M. I., Perrett, K. M., & Bridges, T. J. 2003, *ApJ*, **583**, 752
- Fritz, T. K., Battaglia, G., Pawlowski, M. S., et al. 2018, *A&A*, **619**, A103
- Gaia Collaboration, Brown, A. G. A., Vallenari, A., et al. 2018a, *A&A*, **616**, A1
- Gaia Collaboration, Helmi, A., van Leeuwen, F., et al. 2018b, *A&A*, **616**, A12
- Gifford, D., Miller, C., & Kern, N. 2013, *ApJ*, **773**, 116
- Guo, Q., White, S., Boylan-Kolchin, M., et al. 2011, *MNRAS*, **413**, 101
- Han, J., Cole, S., Frenk, C. S., & Jing, Y. 2016a, *MNRAS*, **457**, 1208
- Han, J., Wang, W., Cole, S., & Frenk, C. S. 2016b, *MNRAS*, **456**, 1017
- . 2016c, *MNRAS*, **456**, 1003
- Han, J., Wang, W., & Li, Z. 2019, arXiv:1909.02690
- Hunter, J. D. 2007, *CSE*, **9**, 90
- Jethwa, P., Erkal, D., & Belokurov, V. 2018, *MNRAS*, **473**, 2060
- Kallivayalil, N., Sales, L. V., Zivick, P., et al. 2018, *ApJ*, **867**, 19
- Lange, J. U., van den Bosch, F. C., Zentner, A. R., Wang, K., & Villarreal, A. S. 2019, *MNRAS*, **482**, 4824
- Li, Z.-Z., Jing, Y. P., Qian, Y.-Z., Yuan, Z., & Zhao, D.-H. 2017, *ApJ*, **850**, 116
- Lokas, E. L. 2002, *MNRAS*, **333**, 697
- Lynden-Bell, D. 1967, *MNRAS*, **136**, 101
- Mamon, G. A., Biviano, A., & Boué, G. 2013, *MNRAS*, **429**, 3079
- More, S., Kravtsov, A. V., Dalal, N., & Gottlöber, S. 2011, *ApJS*, **195**, 4

- Navarro, J. F., Frenk, C. S., & White, S. D. M. 1996, *ApJ*, **462**, 563
- Newton, O., Cautun, M., Jenkins, A., Frenk, C. S., & Helly, J. C. 2018, *MNRAS*, **479**, 2853
- Old, L., Wojtak, R., Mamon, G. A., et al. 2015, *MNRAS*, **449**, 1897
- Oliphant, T. E. 2007, *CSE*, **9**, 10
- Pace, A. B., & Li, T. S. 2019, *ApJ*, **875**, 77
- Patel, E., Besla, G., Mandel, K., & Sohn, S. T. 2018, *ApJ*, **857**, 78
- Posti, L., Binney, J., Nipoti, C., & Ciotti, L. 2015, *MNRAS*, **447**, 3060
- Pratt, G. W., Arnaud, M., Biviano, A., et al. 2019, *SSRv*, **215**, 25
- Price, D. J. 2012, *JCoPh*, **231**, 759
- Richings, J., Frenk, C., Jenkins, A., et al. 2018, arXiv:1811.12437
- Rines, K., & Diaferio, A. 2006, *AJ*, **132**, 1275
- Saro, A., Mohr, J. J., Bazin, G., & Dolag, K. 2013, *ApJ*, **772**, 47
- Sawala, T., Pihajoki, P., Johansson, P. H., et al. 2017, *MNRAS*, **467**, 4383
- Serra, A. L., Diaferio, A., Murante, G., & Borgani, S. 2011, *MNRAS*, **412**, 800
- Simon, J. D. 2019, *ARA&A*, **57**, 375
- Sohn, S. T., Watkins, L. L., Fardal, M. A., et al. 2018, *ApJ*, **862**, 52
- Spergel, D. N., Verde, L., Peiris, H. V., et al. 2003, *ApJS*, **148**, 175
- Tempel, E., Tamm, A., Gramann, M., et al. 2014, *A&A*, **566**, A1
- van der Walt, S., Colbert, S. C., & Varoquaux, G. 2011, *CSE*, **13**, 22
- Vasiliev, E. 2019, *MNRAS*, **484**, 2832
- Wang, W., Han, J., Cole, S., Frenk, C., & Sawala, T. 2017, *MNRAS*, **470**, 2351
- Wang, W., Han, J., Cole, S., et al. 2018, *MNRAS*, **476**, 5669
- Wang, W., Han, J., Cooper, A. P., et al. 2015, *MNRAS*, **453**, 377
- Watkins, L. L., Evans, N. W., & An, J. H. 2010, *MNRAS*, **406**, 264
- Watkins, L. L., van der Marel, R. P., Sohn, S. T., & Evans, N. W. 2019, *ApJ*, **873**, 118
- Wechsler, R. H., & Tinker, J. L. 2018, *ARA&A*, **56**, 435
- Wilkinson, M. I., & Evans, N. W. 1999, *MNRAS*, **310**, 645
- Williams, A. A., & Evans, N. W. 2015, *MNRAS*, **448**, 1360
- Wojtak, R., Łokas, E. L., Mamon, G. A., & Gottlöber, S. 2009, *MNRAS*, **399**, 812
- Wojtak, R., Łokas, E. L., Mamon, G. A., et al. 2008, *MNRAS*, **388**, 815
- Wojtak, R., Old, L., Mamon, G. A., et al. 2018, *MNRAS*, **481**, 324
- Wolf, J., Martinez, G. D., Bullock, J. S., et al. 2010, *MNRAS*, **406**, 1220
- Zhai, M., Xue, X.-X., Zhang, L., et al. 2018, *RAA*, **18**, 113
- Zhu, Q., Marinacci, F., Maji, M., et al. 2016, *MNRAS*, **458**, 1559